Chemical
Science

EDGE ARTICLE

Qingyun Wan, Chi-Ming Che *et al.*

³MMLCT excited states of luminescent binuclear Pd^{II} complexes: excited state inner-sphere electron-transfer reactions and application

15 YEARS ANNIVERSARY

Cite this: *Chem. Sci.*, 2025, **16**, 10701

3MMLCT excited states of luminescent binuclear PdII complexes: excited state inner-sphere electron-transfer reactions and application†

Minying Xue,[ab] Wai-Pong To, [a] Gang Cheng, [abc] Yuzhen Zhang, [d] Zhou Tang,[a] Lili Du,[e] Kam-Hung Low, [a] Qingyun Wan*[f] and Chi-Ming Che [*abc]

Compared with PtII analogues that exhibit unique stimulus-induced switching luminescence properties and novel material applications, the properties and reactivity of the 3MMLCT excited state of PdII complexes in solutions are under-developed. Here, we prepared a series of binuclear cyclometalated PdII complexes with short intramolecular Pd–Pd distances of 2.79–2.89 Å and luminescent 3MMLCT excited states in solutions at 298 K (emission quantum yield and radiative decay rate constant up to 0.70 and 2×10^5 s^{-1}, respectively). Their photophysical properties have been examined by femtosecond time-resolved absorption spectroscopy, and the 1e oxidation products of binuclear PdII complexes have been studied by electron paramagnetic resonance spectroscopy and computational studies. Density functional theory (DFT) and time-dependent DFT (TDDFT) calculations show that changing the C-deprotonated aryl pyridine (C^N) ligand to the strong σ-donor aryl N-heterocyclic carbene (C^C*) ligand significantly increases the energy level of the metal centered (3dd) excited state. The binuclear PdII complex with a redox-active formamidinate bridging ligand reacts with benzyl bromide to immediately generate PdII–PdIII–Br species upon light irradiation. Quenching and time-resolved absorption experiments show that the PdII–3MMLCT excited state reacts with alkyl bromides via an inner-sphere electron transfer pathway. These binuclear PdII complexes were examined as organic light-emitting diode (OLED) emitters and photocatalysts for C–C bond formation reactions.

Introduction

The metal–metal-to-ligand charge transfer [also defined as MMLCT or (dσ* → π*)] excited state of d^8 metal complexes, taking the PtII–3MMLCT excited state as an example, exhibits unique photophysical properties and reactivity.[1] This type of excited state usually exhibits luminescence properties that can be reversibly switched by external stimulus,[2] as well as a large radiative decay rate constant ($k_r \approx 10^5$–10^6 s^{-1}) and low emission energy.[3] In addition, due to the presence of axial vacant coordination sites, the 3MMLCT excited state is reactive towards the activation of C–X bonds through the inner-sphere atom transfer or electron transfer mechanism.[4] We are interested in developing the photochemistry of binuclear PdII complexes through the 3MMLCT excited state, which reacts with C–X bonds to produce reactive PdIII species (PdIII–PdII–X or X–PdIII–PdIII–X). Compared to Pt analogues, these PdIII–PdII–X or X–PdIII–PdIII–X species are rarely studied and reported. PdIII species are generally reactive and unstable, and can be easily reduced back to PdII,[5] suggesting that luminescent binuclear PdII complexes with long-lived 3MMLCT excited states can be more reactive photocatalysts. In the literature, only a few binuclear PdII complexes with long-lived luminescent 3MMLCT excited states in solution have been reported.[6] The small ligand-field splitting of the PdII ion results in a low-lying metal-centered 3dd excited state that is more thermally accessible than in the PtII ion, thus allowing efficient non-radiative decay through electron population in the antibonding $4d_{x^2-y^2}$ orbital.[7] To destabilize the dd excited state, researchers have employed strong-field C-deprotonated tridentate or tetradentate cyclo-metalated ligands to form luminescent PdII complexes,[8] or used σ-donating diarylacetylide bridging ligands to construct discrete binuclear PdII complexes.[6a]

State Key Laboratory of Synthetic Chemistry, Department of Chemistry, The University of Hong Kong, Pokfulam Road, Hong Kong, P. R. China. E-mail: cmche@hku.hk

Hong Kong Quantum AI Lab Limited, Hong Kong Science Park, Units 909–915, Building 17W, Science Park West Avenue, Pak Shek Kok, Hong Kong, P. R. China

HKU Shenzhen Institute of Research and Innovation, Shenzhen, Guangdong, P. R. China

School of Chemistry and Chemical Engineering, Guangxi Minzu University, No. 158, Daxue West Road, Nanning, Guangxi, P. R. China

School of Life Science, Jiangsu University, Zhejiang, P. R. China

Department of Chemistry, The Chinese University of Hong Kong, Shatin, Hong Kong, P. R. China. E-mail: qingyunwan@cuhk.edu.hk

† Electronic supplementary information (ESI) available. CCDC 1976305, 2018758, 2053114, 2353065, 2353067 and 2353099. For ESI and crystallographic data in CIF or other electronic format see DOI: https://doi.org/10.1039/d4sc08612k

We describe here the synthesis, photophysical and photochemical properties of a series of binuclear Pd^{II} complexes (**1–7**) and two Pt^{II} counterparts (**Ref-Pt1** and **Ref-Pt5**[3c]). Complexes **1** and **3–7** have short intramolecular Pd–Pd distances of 2.79–2.89 Å. Binuclear Pd^{II} complexes with cyclometalated [C^C*] (aryl N-heterocyclic carbene) ligands exhibit strong ^{3}MMLCT emissions in dilute solution, solid state and PMMA thin films. Based on DFT/TDDFT calculations, two factors affecting the photophysical properties of binuclear Pd^{II} complexes include (1) the relative energy of the ^{3}dd excited state compared to the lowest ^{3}MMLCT state, which is closely related to the non-radiative decay process (k_{nr}); (2) radiative decay process, affected by the spin–orbit coupling constant of Pd atoms. Upon photo-irradiation, the binuclear Pd^{II} complex with DPF bridging ligand (DPF = N,N'-diphenylformamidinate) activates alkyl bromides through the inner-sphere type electron transfer pathway, to produce Pd^{II}–Pd^{III}–Br species. A binuclear Pd^{II} complex in this work was also shown to be a photosensitizer or photocatalyst for C–C bond coupling reactions. OLEDs fabricated using binuclear Pd^{II} complexes exhibit high maximum luminance and external quantum efficiency (EQE) up to 104 000 cd m^{-2} and 22.9%, respectively.

Results and discussion

Synthesis and characterization

The structures of the binuclear Pd^{II} complexes (**1–7**) and Pt^{II} analogues (**Ref-Pt1** and **Ref-Pt5**) are shown in Fig. 1. Their syntheses and characterization data are given in the ESI.† Complexes **1** and **2** were prepared by the reaction of $[Pd(C^N)(\mu\text{-}OAc)]_2$ (C^N = 2-[1,1′-biphenyl]-3-yl-4-phenylpyridine) with pyrazole (Pz) ligands and NaOMe in THF. The Pt^{II} analogue **Ref-Pt1** was similarly prepared from $[Pt(C^N)(\mu\text{-}Cl)]_2$. These complexes were purified by crystallization to give a mixture of *cis* and *trans* isomers (Fig. 1a), as shown by ^{1}H NMR (see the ESI†). Complex **3** was prepared by treating $[Pd(C^N)(\mu\text{-}Cl)]_2$ with DPF ligand and KO^tBu in N,N-dimethylformamide (DMF), while **4–7** and **Ref-Pt5** were synthesized by a one-pot reaction; the $[M(C^C*)(\mu\text{-}Cl)]_2$ (M

= Pd or Pt) was generated *in situ* through transmetalation between silver carbene intermediate and $Pd(COD)Cl_2$ or $Pt(COD)Cl_2$. The products were purified by column chromatography to give complexes **3–7** and **Ref-Pt5** as pure *trans* isomers in moderate yields (15–40%). All binuclear Pd^{II} complexes were obtained as air-stable light green to orange solids, and **Ref-Pt1** and **Ref-Pt5** are red solids. In the absence of light, complex **5** shows higher stability than complex **1** in aerated CH_2Cl_2 and toluene; the former is stable for at least a week while the latter decomposed after one day (Fig. S7 and S8†).

The crystal structures of complexes **1–5** and **Ref-Pt1** are shown in Fig. 1b. Complex **2** shows a boat-shaped conformation, similar to that reported for $[(ppy)Pd(\mu\text{-}Pz)]_2$ (Hppy = 2-phenylpyridine) with the same unsubstituted Pz ligand.[9] The other complexes adopt a "double decker" conformation in which the bridging ligand is orthogonal to the plane containing the Pd/Pt atom and the cyclometalated ligand. From their crystal structures, **2** and **Ref-Pt1** exhibit the *cis* configuration. On the other hand, complex **1** shows the *trans* configuration in its crystal structure. As the steric bulk of the bridging Pz ligand increases, the Pd–N(Pz)–N(Pz) angle decreases from 119.8° in **2** to 108.5° in **1**, resulting in a shortening of the Pd–Pd distance from 3.40 Å in **2** to 2.79 Å in **1**. A similar finding was reported by Ma *et al.* in analogous binuclear Pt^{II} complexes.[10] **Ref-Pt1**, which has the same ligand scaffold as **1**, also exhibits a close Pt–Pt distance of 2.90 Å. Complexes **3–5** with bridging DPF ligands have short intramolecular Pd–Pd distances of 2.86–2.89 Å and are in the *trans* configuration.

Absorption and emission spectroscopy

The electronic absorption spectra of binuclear Pd^{II} complexes, **Ref-Pt1**, and **Ref-Pt5** are shown in Fig. 2a, b and S5.† The spectral data are summarized in Table 1. In CH_2Cl_2, complexes **1**, **2**, and **Ref–Pt1** show an intense absorption band with λ_{max} at 268–279 nm ($\varepsilon > 10^4$ M^{-1} cm^{-1}) and a less intense absorption band at 356–385 nm ($\varepsilon = 5.8 - 7.3 \times 10^3$ M^{-1} cm^{-1}). Both bands
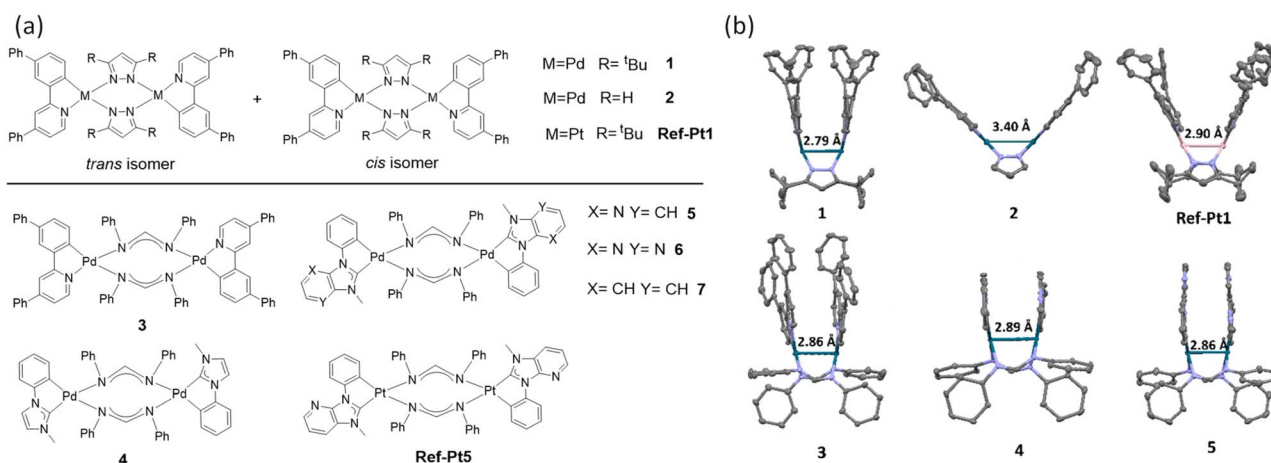

Fig. 1 (a) Chemical structures of binuclear Pd^{II} and Pt^{II} complexes in this work. (b) Crystal structures of complexes **1–5** and **Ref-Pt1** (hydrogen atoms are omitted for clarity).
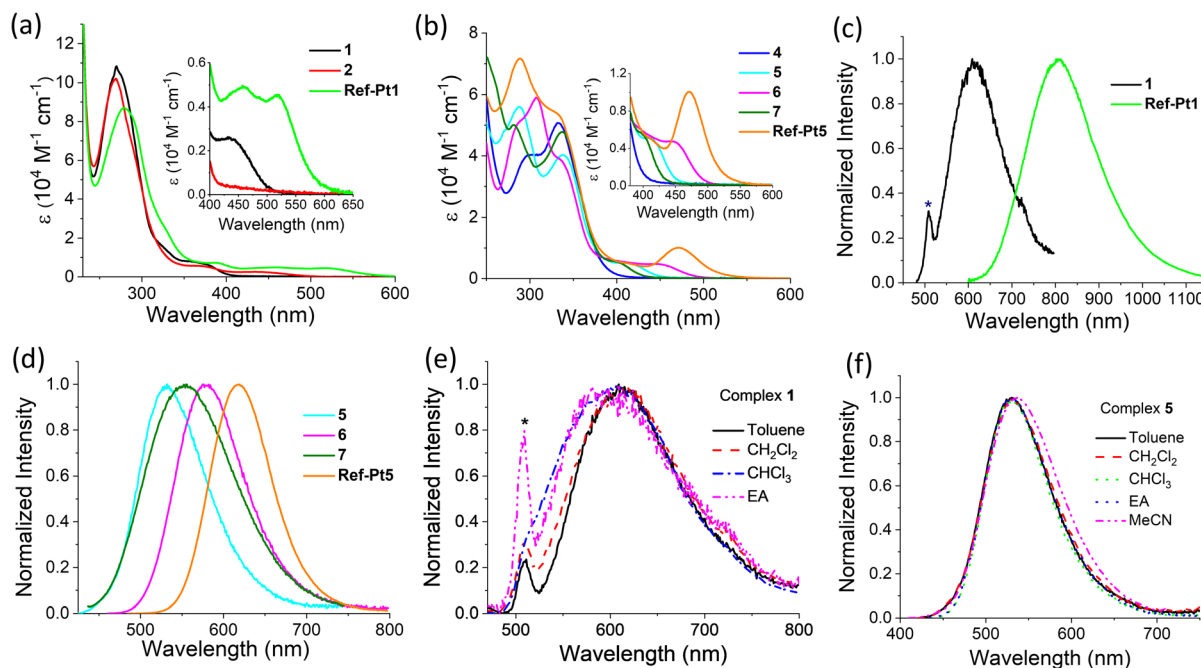
Fig. 2 Absorption spectra of (a) complexes **1**, **2**, and **Ref-Pt1**, (b) complexes **4–7** and **Ref-Pt5** in CH_2Cl_2 at RT. Emission spectra of (c) complexes **1** and **Ref-Pt1**, (d) complexes **5–7** and **Ref-Pt5** in deoxygenated CH_2Cl_2 (2×10^{-5} M) at RT. Emission spectra of (e) complexes **1** and (f) **5** in various solvents. Asterisk (*) indicates Raman scattering of excitation light.

were assigned to (π–π*) singlet intraligand (^{1}IL) transitions localized on the cyclometalated C^N ligand. For **1**, there is an additional weak absorption band with λ_{max} at 433 nm ($\varepsilon = 2.8 \times 10^3$ M^{-1} cm^{-1}), and this band is blue-shifted relative to **Ref-Pt1** (λ_{max} = 518 nm). These low-energy absorption bands are attributed to the $[d\sigma^*(Pd_2/Pt_2) \rightarrow \pi^*(C^N)]$ ^{1}MMLCT transition, as shown by the DFT calculations (*vide infra*). For **3–7**, the intense absorption bands at 242–358 nm ($\varepsilon > 10^4$ M^{-1} cm^{-1}) were assigned to (π–π*) ^{1}IL transition of the C^N/C^C* or DPF ligands.

Complexes **3** and **5–7** show a broad shoulder band tailing to 500 nm ($\varepsilon = 2.0 – 5.5 \times 10^3$ M^{-1} cm^{-1}), which was assigned to a mixed $[\pi(DPF) \rightarrow \pi^*(C^N/C^C^*)]$ ^{1}LLCT (major) and $[d\sigma^*(Pd_2) \rightarrow \pi^*(C^N/C^C^*)]$ ^{1}MMLCT (minor) transitions (see DFT calculations). The energy of these low-energy absorption bands follows the order **7** > **5** > **6**, which is related to the energy level of the π^* orbitals of the C^C* ligand. The high energy level of π^* orbitals of the non-conjugated C^C* ligand of **4** causes its ^{1}LLCT/^{1}MMLCT transitions to occur in the region <400 nm. The low-energy absorption bands (λ_{max} > 400 nm) of **1** and **5** show

Table 1 UV-visible absorption and emission data of complexes **1–7**, **Ref-Pt1**, and **Ref-Pt5** in CH_2Cl_2, solid state and 2 wt% PMMA thin films

	UV-vis absorption[a]	Emission at 298 K		
		λ_{em} [nm] (τ^d [μs]; Φ_{em} [%]; $k_r{}^i$ [10^3 s^{-1}]; $k_{nr}{}^j$ [10^4 s^{-1}])		
	λ_{max} [nm] (ε [10^3 M^{-1} cm^{-1}])	In deoxygenated $CH_2Cl_2{}^b$	Solid state[c]	2 wt% in PMMA[c]
1	269 (102.1), 365 (sh, 5.9), 433 (br, 2.8)	609 (0.30; 0.016[e]; 0.53; 333)	612 (4.8; 30; 63; 15)	592 (7.1; 3.0; 4.2; 14), 736 (sh)
2	269 (102.2), 356 (sh, 5.8)	Non-emissive	497 (sh), 521 (0.11; <0.1; n.d.; n.d.)	479, 506 (0.29; <0.1; n.d.; n.d.)
3	268 (119.7), 358 (24.9), 463 (br, 2.0)	595 (0.88; 2.0[f]; 23; 111)	585 (6.3; 38; 60; 9.8)	583 (9.8; 2.0; 2.0; 10)
4	242 (sh, 75.5), 293 (38.9), 332 (50.7)	Non-emissive	589 (63.9; 70; 11; 0.47)	579 (30.8; 29; 9.4; 2.3)
5	286 (55.7), 338 (40.2), 410 (br, 5.0)	532 (0.45; 3.0[f]; 67; 216)	550 (6.2; 45; 73; 8.9)	519 (7.4; 47; 64; 7.2)
6	286 (sh, 50.5), 307 (59.0), 335 (38.8), 450 (br, 4.7)	576 (5.9; 61[f]; 103; 6.6)	566 (0.25; 5.0; 200; 380)	559 (6.7; 67; 100; 4.9)
7	281 (50.1), 337 (47.8), 400 (5.5)	555 (0.062; 0.15[e]; 24; 1610)	510 (3.8[h]h; 27; 71; 19)	541 (12.9; 58; 45; 3.3)
Ref-Pt1	279 (86.9), 385 (7.3), 460 (4.9), 518 (4.5)	806 (0.14; 8.7[g]; 621; 652)	661 (0.88; 46; 523; 61)	663 (0.76; 31; 408; 91)
Ref-Pt5	288 (58.6), 328 (sh, 43.6), 472 (br, 8.1)	619 (1.4; 62[f]; 443; 27)	628 (1.4; 52; 371; 34)	607 (1.7; 99; 582; 0.59)

[a] At a concentration of 1×10^{-5} M. [b] At a concentration of 2×10^{-5} M. [c] Measured in air. [d] Emission lifetime. [e] Emission quantum yield was calculated using [Ru(bpy)$_3$](PF$_6$)$_2$ as reference (bpy = 2,2'-bipyridyl, in MeCN, Φ_{em}: 0.062, λ_{em} = 619 nm). [f] Emission quantum yield was obtained by integrating sphere. [g] Emission quantum yield was calculated using [Pt(tptbp)] as reference (H$_2$tptbp = tetraphenyltetrabenzoporphyrin, in toluene, Φ_{em}: 0.51, λ_{em} = 770 nm). [h] Weighted average lifetime for biexponential decay. [i] Radiative decay rate constant estimated from the equation $k_r = \Phi_{em}/\tau$. [j] Non-radiative decay rate constant estimated from the equation $k_{nr} = (1 - \Phi_{em})/\tau$.

hypsochromic shifts of up to 13 nm with increasing solvent polarity (Fig. S6 and Table S7†), further indicating the charge transfer nature of these absorption bands.

All complexes, except **2** and **4**, show emission in deoxygenated CH_2Cl_2 at room temperature (RT) (Fig. 2c, d and Table 1). For the binuclear Pd[II] complex, an unstructured emission band is observed with λ_{max} at 532–609 nm and τ in the sub-microsecond regime. The λ_{max} of **1** (609 nm) undergoes a hypsochromic shift from its Pt[II] counterpart **Ref-Pt1** (806 nm), consistent with the spectral assignment of the emission of **1** to $[d\sigma^*(Pd_2) \rightarrow \pi^*(C\char`\^N)]$ [3]MMLCT excited state. The k_r of **1** with τ of 0.30 μs and Φ_{em} of <0.01 is small, about 10^2 s^{-1}. Replacing the bridging Pz ligands to DPF ligands increases the Φ_{em} and k_r, as observed in **3** (Φ_{em}: 0.02; k_r: 2.3×10^4 s^{-1}). On the other hand, the Φ_{em} varies greatly (0.0015–0.61) for binuclear Pd[II] complexes with Pd–NHC bonds (**5–7**). Both complexes **5** and **7** have lower Φ_{em} than **6**, which is mainly due to significant non-radiative decay in solution at RT (k_{nr}: 2.2×10^6 s^{-1} [5], 1.6×10^7 s^{-1} [7] vs. 6.6×10^4 s^{-1} [6]). The emissions of complexes **3** and **5–7** were assigned to a mixed $[d\sigma^*(Pd_2) \rightarrow \pi^*(C\char`\^N/C\char`\^C^*)]$ [3]MMLCT and $[\pi(DPF) \rightarrow \pi^*(C\char`\^N/C\char`\^C^*)]$ [3]LLCT excited state. As the solvent polarity increases from toluene, through CH_2Cl_2, CHCl$_3$ and EA to MeCN, the emission λ_{max} of **1** shows a hypsochromic shift of up to 11 nm (Fig. 2e). In contrast, the emission λ_{max} of **5** is bathochromic shifted by up to 7 nm (Fig. 2f). These shifts suggest that the differences in dipole changes between the ground and excited states of **1** and **5** are opposite. The emission of complex **1** is too weak to be detected in MeCN, and the Φ_{em} of complex **5** drops from 0.043 in toluene to 0.007 in MeCN (Table S7†).

Complexes **1** and **3–7** show broad emission bands with λ_{max} at 510–612 nm in 2 wt% PMMA thin films and in the solid state at RT (Fig. S9 and S10†). In contrast, the emission band of **2** shows a vibronic structure with the first vibronic peak at 479–497 nm attributed to the $[\pi-\pi^*]$ [3]IL excited state. Complexes **1** and **3–7** have Φ_{em} spanning from 0.05 to 0.70, and τ in the microsecond regime, revealing large k_r from 10^4 s^{-1} to 2×10^5 s^{-1}, all of which are significantly larger than the k_r of **2** ($\leq 10^3$ s^{-1}) and other reported Pd[II] complexes with ligand-centered excited states.[11]

Variable-temperature emission decay lifetime

The binuclear Pd[II] complexes (**1**, **3**, **5**, and **7**) exhibit weak emissions in dilute solutions at 298 K with low Φ_{em} (≤ 0.03) and large k_{nr} values ($1.1 - 16.1 \times 10^6$ s^{-1}). In this regard, the variation of τ_{obs} over a large temperature range provides information on the radiationless decay process of the emitting excited state(s) and could be modelled by eqn (1):[12]

$$k_{obs} = k_r + k_{nr} + k_{nr}(T) = k_0 + A \exp\left(\frac{-E_a}{k_B T}\right) \quad (1)$$

where k_0 is the temperature-independent decay rate of the decay process, A is the pre-exponential factor of the Arrhenius term that contributes to the non-radiative process, E_a is the activation energy, and k_B is the Boltzmann constant. To gain insight into the non-radiative processes of the binuclear Pd complexes, the
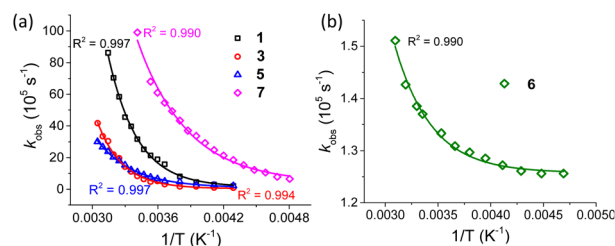

Fig. 3 Plots of the temperature dependence of the excited-state decay rate constant (k_{obs}) of (a) complexes **1** (5×10^{-5} M), **3**, **5**, and **7** (2×10^{-5} M) and (b) **6** (2×10^{-5} M) in deoxygenated toluene.

Table 2 Kinetic parameters for excited-state deactivation

Complex	k_0 [s^{-1}]	A_1 [s^{-1}]	E_a [cm^{-1}]
1	144 852	1.08×10^{12}	2605
3	37 601	2.05×10^{12}	2989
5	96 000	2.81×10^{10}	2088
6	125 769	1.73×10^8	1994
7	406 039	1.56×10^{10}	1520

temperature-dependent emission lifetimes of complexes **1**, **3**, and **5–7** were measured in deoxygenated toluene. As shown in Fig. 3, using eqn (1), the k_{obs} values fit well with $1/T$. Complexes **1** and **3** have similarly large A values, about 10^{12} s^{-1} (Table 2), but the E_a value of **3** (2989 cm^{-1}) is slightly larger than that of **1** (2605 cm^{-1}). This is consistent with the higher Φ_{em} and smaller k_{nr} of **3** compared to **1** in dilute solutions (Table 1). In particular, the A values for **1** and **3** are approximately 10^{11}–10^{14} s^{-1}, suggesting the existence of an activated and rate-determining surface crossing mechanism to reach higher-lying dark electronic state based on previous studies on luminescent d^6 and d^8 metal complexes.[13] Although the A values of **5** (2.81×10^{10} s^{-1}) and **7** (1.56×10^{10} s^{-1}) are about two orders of magnitude smaller than those of **1** and **3**, the E_a values of **5** (2088 cm^{-1}) and **7** (1520 cm^{-1}) make the thermal deactivation process non-negligible. Despite having a similar E_a value to complex **5**, the pre-exponential term of complex **6** is significantly smaller ($A = 1.73 \times 10^8$ s^{-1}), which allows moderately efficient emission to occur at RT. The kinetic parameters of complexes **1**, **3**, **5**, and **7** (Table 2) reveal an overwhelming contribution (92–97%) of the temperature-dependent non-radiative decay rate $k_{nr}(T)$ to k_{obs} at 298 K. For **6**, only 8.2% of the k_{obs} come from the $k_{nr}(T)$ term. This is in sharp contrast to complexes **1**, **3**, **5**, and **7**, whose excited states undergo significant thermal populated deactivation processes, resulting in these four complexes having lower Φ_{em} and large k_{nr} in dilute solutions at 298 K.

Time-resolved absorption and emission spectroscopy

Complexes **1** and **5** were selected as representative examples to study the excited-state dynamics of binuclear Pd[II] complexes by femtosecond/nanosecond time-resolved absorption difference (fs/ns-TA) and femtosecond time-resolved fluorescence (fs-TRF) spectroscopy. In toluene, different excited state kinetics were observed for the two complexes. The initial TA ($\sim$0.8 ps) of **1** has
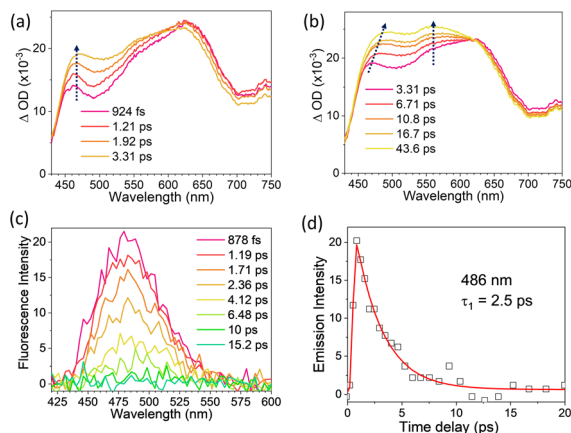
Fig. 4 (a) and (b) fs–TA spectra of **5** at selected time delays; (c) fs–TRF spectra and (d) its kinetic trace of **5** in toluene.

Fig. 5 Cyclic voltammograms of selected complexes in CH_2Cl_2 for anodic sweeps and in DMF for cathodic sweeps with 0.1 M NBu_4PF_6 as electrolyte. $E_{1/2}$ ($Cp_2Fe^{+/0}$) was recorded in the range of 0.43–0.52 V vs. SCE in CH_2Cl_2 or DMF.

two excited-state absorption (ESA) signals at 509 and 610 nm that decay throughout the delay time (0.8 ps–2.5 ns; Fig. S11a†). The kinetics at 509 nm showed two ps decay time constants of 1.1 and 8.8 ps (Fig. S11b†); the former is consistent with TRF decay (τ_{TRF}: 1.0 ps; Fig. S12b†). For **5**, its initial TA ($\sim$0.9 ps) is characterized by two ESA signals at 462 and 625 nm (Fig. 4a). The spectral evolution of **5** occurs in three stages. The early phase occurs with a time constant of 2.0 ps and involves an ESA growth at 462 nm. This 2.0 ps time constant is consistent with the TRF decay (τ_{TRF}: 2.5 ps; Fig. 4c and d). In the second stage, with a time constant of 13.8 ps, the TA rises at 462 and 560 nm, with the former undergoing an 18 nm redshift (Fig. 4b). After the second stage of TA evolution, the fs-TA signals undergo a long-lived decay process on the ns timescale to give a TA spectrum consistent with the respective ns-TA spectrum (Fig. S13b†), which can be attributed to the formation of T_1 state. Based on these time-resolved spectroscopic measurements, the excited state cascades of complexes **1** and **5** were constructed (Fig. S14†). Upon excitation, the emission λ_{max} of the S_1 excited state is at 521 nm for **1** (Fig. S12a†) and 486 nm for **5** (Fig. 4c), both of which are depleted by S_1-to-triplet (T_n or T_1) intersystem crossing (ISC) with an ultrafast time constant (1.1 ps for **1**; 2.0 ps for **5**). The formed triplet excited state undergoes an internal conversion from T_n to T_1 or vibrational cooling of T_1 with time constants of 8.8 ps for **1** and 13.8 ps for **5**. This is followed by radiative decay to the ground state in a sub-microsecond timescale (Table 1).

Electrochemistry

The electrochemical properties of complexes **1–7**, **Ref-Pt1**, and **Ref-Pt5** were investigated by cyclic voltammetry (CV). To avoid undesirable side reactions between oxidized species and coordinating solvent molecules, the non-coordinating solvent CH_2Cl_2 was used for anodic scanning.[14] Cathodic scanning was performed in DMF due to its wide electrochemical window for reduction. The CV curves and electrochemical data are shown in Fig. 5, S15† and Table 3, respectively. Complex **1** exhibits a reversible oxidation couple with $E_{1/2}$ at 0.86 V vs. SCE, while **2** shows an irreversible oxidation wave with E_{pa} at 1.22 V vs. SCE.
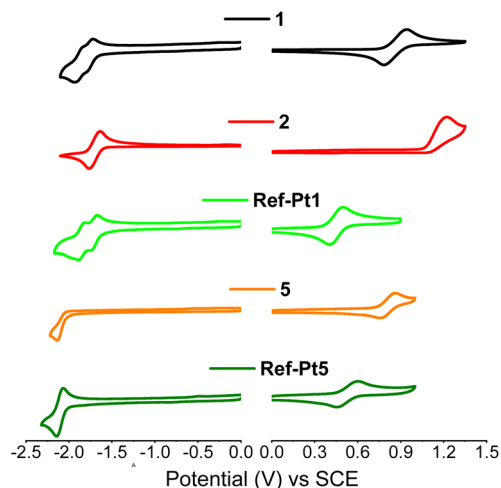
This is consistent with the HOMO of **1** being destabilized by metal–metal interactions. Complexes **3–7** show reversible/quasi-reversible oxidation couple with $E_{1/2}$ at 0.72–0.87 V vs. SCE. Compared to their Pt^{II} analogues **Ref-Pt1** and **Ref-Pt5**, the $E_{1/2}$ values of **1** and **5** are anodically shifted by 0.42 and 0.29 V, respectively (Fig. 5). Based on the DFT calculations (vide infra), the oxidation process of complex **1** is assigned to be metal-centered, whereas the oxidation process of complex **5** occurs on the DPF ligand. For the reduction process, complexes **1**, **3**, **6**, and **Ref-Pt1** exhibit two reversible reduction couples with $E_{1/2}$ ranging from -1.68 to -1.79 and -1.82 to -2.04 V vs. SCE, respectively, while **2** exhibits one reversible reduction couple with $E_{1/2}$ at -1.70 V vs. SCE. The reduction process of complexes **4**, **5**, **7**, and **Ref-Pt5** is irreversible with E_{pc} spanning from -2.11 to -2.73 V vs. SCE. The reduction potentials of binuclear Pd^{II} complexes **1–7** vary with the cyclometalated ligands. Also pairs of binuclear complexes with the same cyclometalated and bridging ligands have similar reduction potentials, such as complex **1** ($E_{1/2} = -1.72$ vs. SCE) and **Ref-Pt1** ($E_{1/2} = -1.68$ vs. SCE), or complex **5** ($E_{pc} = -2.17$ V vs. SCE) and **Ref-Pt5** ($E_{1/2} = -2.11$ V vs. SCE). This result shows that the reduction of the binuclear Pd^{II} complex in this study is mainly ligand centered.

DFT/TDDFT calculations

DFT/TDDFT calculations were performed on the binuclear Pd^{II} complex **1** and its Pt^{II} counterpart **Ref-Pt1** to study their electronic structures in the ground and excited states. Because both trans and cis isomers were observed in the ^1H NMR spectra of **1** and **Ref-Pt1**, calculations were performed for both isomers. A small energy difference (ranging from 0.04 to 0.06 eV) was observed between the cis and trans isomers (Table S8†). Since calculations for the cis and trans isomers show no significant differences, only the complexes with the trans geometry are described here. The optimized geometries of **1** and **Ref-Pt1** match well with their crystal structures, as shown in Fig. 6a,

Table 3 Electrochemical data[a] and excited-state redox properties

Complex	$E(M^+/M^0)$ [V]	$E(M^0/M^-, M^-/M^{2-})$ [V]	E_{0-0}[e] [V]	$E(M^+/*M^0)$[f] [V]	$E(*M^0/M^-)$[f] [V]
1	0.86[b]	−1.72, −1.84[b]	2.26	−1.40	0.42
2	1.22[c]	−1.70[b]	—	—	—
3	0.86[b]	−1.79, −2.04[b]	2.40	−1.54	0.67
4	0.72[b]	−2.73[d]	—	—	—
5	0.81[b]	−2.17[d]	2.69	−1.88	0.52
6	0.87[b]	−1.68, −1.82[b]	2.45	−1.58	0.80
7	0.78[b]	−2.27[d]	2.67	−1.89	0.40
Ref-Pt1	0.44[b]	−1.68, −1.83[b]	1.83	−1.39	0.15
Ref-Pt5	0.52[b]	−2.11[b]	2.25	−1.73	0.10

[a] Measured in CH_2Cl_2 for anodic sweeps and DMF for cathodic sweeps with 0.1 M NBu_4PF_6 as supporting electrolyte at a scan rate of 100 mV s^{-1}; $E_{1/2}$ ($Cp_2Fe^{+/0}$) is recorded at the range of 0.43–0.52 V $vs.$ SCE in CH_2Cl_2 or DMF. [b] Values refer to $E_{1/2}$ $versus$ SCE. [c] Value refers to the anodic peak $versus$ SCE. [d] Value refers to the cathodic peak $versus$ SCE. [e] Approximate zero–zero excitation energy, E_{0-0}, was estimated from the emission onset at 298 K in CH_2Cl_2. [f] Estimation of approximate excited-state redox potentials: $E(M^+/*M^0) = E(M^+/M^0) - E_{0-0}$ (V $vs.$ SCE), $E(*M^0/M^-) = E(M^0/M^-) + E_{0-0}$ (V $vs.$ SCE).

where the intramolecular Pd–Pd and Pt–Pt distances are calculated to be 2.83 Å and 2.87 Å, respectively. In the calculated absorption spectrum (Fig. 6b), the lowest transition band is located at 462 nm for **1** and 530 nm for **Ref-Pt1**, both close to the experimental values (λ_{max}: 440 nm for **1**, 518 nm for **Ref-Pt1**). As the distance between two metal atoms is less than the sum of their van der Waals radii, the overlap between the two valence nd_{z^2} (n = 4 for Pd and 5 for Pt) orbitals will result in the formation of a bonding ($nd\sigma$) and an antibonding ($nd\sigma^*$) orbital. In the MO diagrams shown in Fig. 6c, the HOMOs of both **1** and **Ref-Pt1** consist of the $nd\sigma^*$ orbital between two

metals, while the LUMO is mainly located at the C^N ligand. The calculated S_1 states of **1** and **Ref-Pt1** are derived from the HOMO ($nd\sigma^*$) to LUMO (π^*) transition. The $4d\sigma^*$ orbital energy level of complex **1** is lower than the $5d\sigma^*$ orbital of **Ref-Pt1**, which causes the HOMO–LUMO gap of complex **1** to increase and the lowest absorption band to blue-shift. According to the calculation results, the lowest absorption bands ($S_0 \rightarrow S_1$) of **1** and **Ref-Pt1** are attributed to the ^{1}MMLCT transition, and the calculated oscillator strengths are 0.02 and 0.04, respectively.

The triplet excited state T_1 of **1** and **Ref-Pt1** was also calculated. Calculations show that the M–M distance in the T_1 state
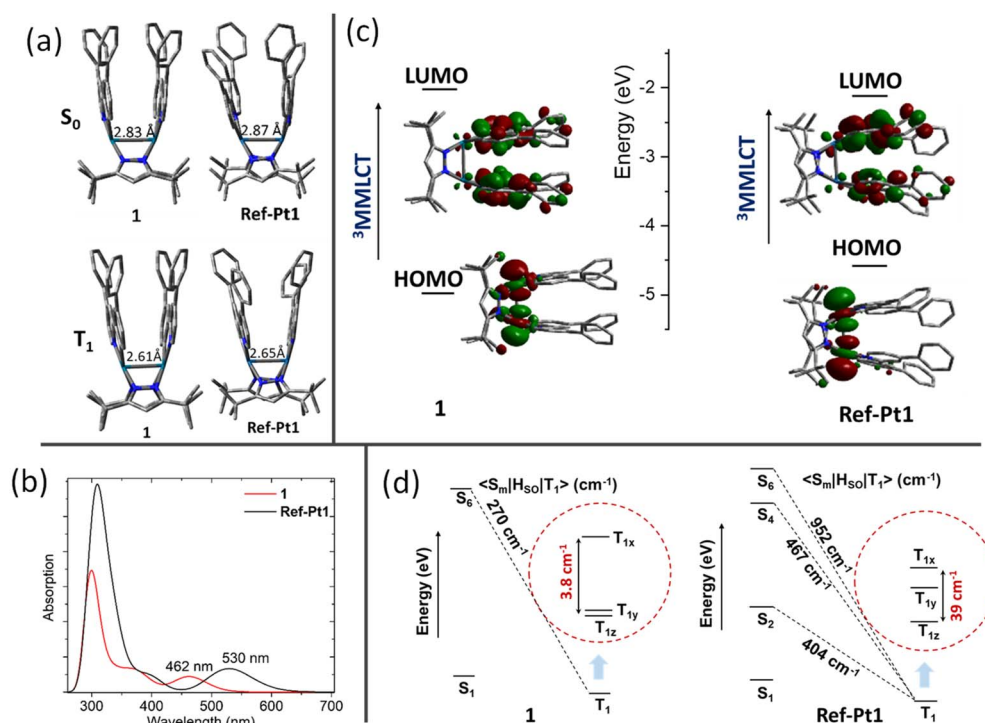

Fig. 6 (a) Optimized structures of **1** and **Ref-Pt1** at S_0 and T_1 state. (b) Calculated absorption spectra of **1** and **Ref-Pt1** based on the optimized S_0 structure. (c) Calculated MO diagrams of **1** and **Ref-Pt1** at T_1 state. (d) Calculated ZFS and SOC coupling of **1** and **Ref-Pt1** at T_1 state.

of **1** is shortened to 2.61 Å and that of **Ref-Pt1** is shortened to 2.65 Å (Fig. 6a). This is due to the M–M bonding interaction formed by excitation of electrons from the antibonding $d\sigma^*$ orbital to the ligand π^* orbital. The calculated emission wavelength of the ^{3}MMLCT excited state of **1** is 632 nm, which is consistent with the experimentally observed emission λ_{max} at 609 nm.

The phosphorescent radiative decay process of **1** and **Ref-Pt1** was evaluated by calculating the values of zero-field splitting (ZFS) and SOC ($\langle S_m|H_{SO}|T_1\rangle$). As shown in Fig. 6d, the calculated ZFS of **Ref-Pt1** (39 cm^{-1}) is larger than that of **1** (3.8 cm^{-1}). The ZFS value is closely related to the SOC constant, which is 1412 and 4000 cm^{-1} for Pd and Pt, respectively. The contribution of metal orbitals in the singlet and triplet excited states also affects ZFS. Compared to **Ref-Pt1**, complex **1** exhibits a reduced contribution of Pd^{II}-4d orbitals in the MMLCT excited state due to the low-lying Pd^{II}-4d orbitals, resulting in a smaller ZFS in the Pd^{II} complex. For **Ref-Pt1**, the SOC between S_2 and T_{1z}, S_4 and T_{1y}, S_6 and T_{1z} states mainly contributes to the $T_1 \rightarrow S_0$ transition (the T_{1x}, T_{1y}, and T_{1z} refer to three T_1 substates), with calculated values (SOC) of 404, 467 and 952 cm^{-1}, respectively (Fig. 6d). For complex **1**, the $T_1 \rightarrow S_0$ transition is mainly contributed by the SOC between S_6 and T_{1x} states, with a value of 270 cm^{-1}, which is smaller than that of **Ref-Pt1**.

DFT/TDDFT calculations were also performed on **5** to examine the effect of DPF ligands on the excited state. In the calculated absorption spectrum (Fig. 7a), the $S_0 \rightarrow S_1$ transition of **5** is located at 418 nm, which is consistent with the experimental observation (λ_{max}: 410 nm). As shown in the MO diagram (Fig. 7c), the HOMO of **5** consists of π orbitals of the DPF ligand (82%) and the LUMO is mainly located at the C^C* ligand. The $4d\sigma^*$ orbital is located in the H-2 orbital. The S_1 state of **5** is mainly contributed by the HOMO $\rightarrow$ LUMO transition, and the H-2 $\rightarrow$ LUMO transition contributes moderately.

Therefore, the lowest absorption band of **5** was assigned to a mixture of ^{1}LLCT/^{1}MMLCT transitions. In the T_1 excited state, the Pd–Pd distance is significantly shortened (Fig. 7b), which lifts the H-2 orbital ($4d\sigma^*$) to the HOMO. The $T_1 \rightarrow S_0$ transition of **5** is mainly contributed by the HOMO $\rightarrow$ LUMO transition. The HOMO of complex **5** at T_1 state contains contributions from both the ligand and the metal, so the T_1 state was assigned as a mixed ^{3}MMLCT/^{3}LLCT excited state.

Since the ligand field splitting of Pd^{II} ions is smaller relative to Pt^{II} ions, the thermal population of the metal centered (^{3}dd) excited state provides a quenching pathway for the emissive ^{3}MMLCT excited state of the binuclear Pd^{II} complex. In this regard, the relative energies between the ^{3}MMLCT and ^{3}dd excited states of complexes **1** and **Ref-Pt1** were calculated (Fig. 7d, S18 and S19†). For complex **1**, the T_1 state consists of 90% ^{3}MMLCT and 10% ^{3}dd characters. The ^{3}dd character also has a major contribution to the T_2 state and the T_1–T_2 energy difference is calculated to be 0.27 eV. In comparison, the ^{3}dd character does not contribute to the T_1 state of **Ref-Pt1**, but has a major contribution to the T_8 state, which has an energy 1.4 eV higher than the T_1 state. These results indicate that the excited-state deactivation process of **1** through the ^{3}dd excited state is thermally more feasible relative to **Ref-Pt1**, leading to a faster non-radiative decay process of **1**. For complexes **5** and **6**, the excited states with dominant ^{3}dd character are the T_5 states at 2.92 and 2.77 eV, respectively (Fig. S20 and S21†). These energies are significantly higher than the T_2 state energy of complex **1**, showing that the incorporation of strong σ-donating NHC ligands can destabilize the ^{3}dd excited state.[15] The calculated T_1–T_5 energy differences of complexes **5** and **6** are 0.66 eV and 0.69 eV, respectively (Fig. 7d), indicating the deactivation pathway through the ^{3}dd state of complexes **5** and **6** is less feasible than for complex **1**.

Fig. 7 (a) Calculated absorption spectrum of **5** (red line) based on the optimized structure, and the experimental absorption spectrum (black line). (b) Optimized structures of complex **5** at ground state (S_0) and triplet excited state (T_1). (c) Calculated MOs diagram of **5** at S_0 (left) and T_1 (right). (d) Calculated ^{3}MMLCT and ^{3}dd excited state energy of complexes **1**, **5**, **6**, and **Ref-Pt1**. Note that due to mixing, the state labels may not strictly apply.

Oxidation of complexes 1 and 5

The UV-vis absorption spectra of **1** (Fig. 8a) and **5** (Fig. 8b) were recorded before and after the addition of the one-electron oxidant tris(4-bromophenyl)ammoniumyl hexachloroantimonate (TBPA)SbCl$_6$ ($E_{1/2}$ = 1.05 V *vs.* SCE). For both complexes, a spectral evolution with attenuation of the low-energy absorption band (λ_{max} = 410–440 nm) and the emergence of new absorption features in the lower energy region (λ = 500–1000 nm) is observed. The spectral transformation is similar to that observed for the two complexes during spectroelectrochemical oxidation (Fig. S16†), although the latter could not recover to its original state due to the instability of the oxidized species under spectroelectrochemical conditions. EPR spectra of reaction mixtures of complexes **1** and **5** with (TBPA) SbCl$_6$ were recorded at 100 K to identify the electronic configuration of the 1e-oxidized species. For the reaction of complex **1** with (TBPA)SbCl$_6$, spectral simulations gave axial g values with $g_\perp$ = 2.240 and $g_\parallel$ = 1.996, and ^{105}Pd hyperfine structures with $A_\perp$ = 53 G and $A_\parallel$ = 45 G (Fig. 8c), showing that the SOMO has dominant d$_{z^2}$ character. The EPR spectrum is similar to that reported for [Pd^{II}Pd^{III}(μ-dpb)$_4$]$^+$.[16] In contrast, the EPR spectrum of **5** after adding (TBPA)SbCl$_6$ showed a typical organic radical signal (g = 2.00) (Fig. 8d), pointing to the ligand-based SOMO.[17] Therefore, the chemical oxidation of **1** with (TBPA)SbCl$_6$ produces [(Pd^{II}–Pd^{III})(Pz$^-$)$_2$]$^{3+}$ (**1$^+$**) species, while the chemical oxidation of **5** produces [(Pd^{II}–Pd^{II})(DPF$^{0.5-}$)$_2$]$^{3+}$ (**5$^+$**) species. The formation of **5$^+$** was also observed in the photoredox reaction of **5** with 4-(methoxycarbonyl)-*N*-methylpyridinium hexafluorophosphate. The excited-state redox potential $E(M^+/^*M^0)$ of **5** is −1.88 V *vs.* SCE (Table 3); therefore, the excited state of **5** can react with 4-(methoxycarbonyl)-*N*-methylpyridinium hexafluorophosphate (E_{red} = −0.78 V *vs.* SCE)[18] through the electron-transfer mechanism (eqn (2)). We recorded ns-TA spectra at 1 μs after

$$\text{(5)} + {}^*[\text{Pd}^{II}(\text{DPF}^-)]_2^{2+} \longrightarrow \text{(5}^+\text{)} + [\text{Pd}^{II}(\text{DPF}^{0.5-})]_2^{3+} \quad (2)$$
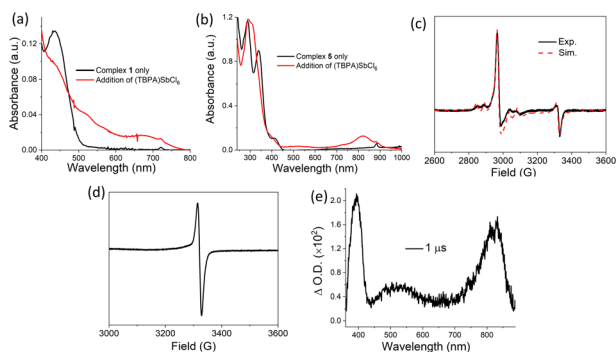
laser excitation of a deoxygenated MeCN/toluene (1 : 9 v/v) solution containing **5** and 4-(methoxycarbonyl)-*N*-methylpyridinium hexafluorophosphate. The spectrum shows absorption bands at 520 and 820 nm (Fig. 8e), similar to the absorption characteristics of **5$^+$** produced by oxidation of **5** with (TBPA) SbCl$_6$ (Fig. 8b). The high-energy absorption band at 398 nm is consistent with the reported spectrum of 4-(methoxycarbonyl)-*N*-methylpyridinyl radical.[18] The 820 nm absorption band follows a bi-exponential decay kinetics with lifetimes of 12.2 and 48.8 μs. Attempts to detect the formation of **1$^+$** under similar photoredox conditions were unsuccessful because the excited state of complex **1** was significantly quenched in MeCN.

Quenching and photochemical studies of complex 5 with alkyl bromides

The quenching of **5**'s phosphorescence by various alkyl bromides was studied in deoxygenated toluene (Fig. S22†). The quenching rate constants (k_q) are listed in Table 4. The k_q value of CBr$_4$ is almost diffusion-controlled, whereas the k_q values for allyl bromide and CH$_2$Br$_2$ are much smaller, about 10^6 M^{-1} s^{-1}. Plots of log k_q values *versus* E_{red} and BDE values of alkyl bromides are shown in Fig. 9a and b. The k_q values correlate better with E_{red} than with BDE values. In order to obtain more spectroscopic evidence of the photoreaction mechanism between **5** and alkyl bromide, the ns-TA spectrum of laser flash photolysis (the excitation wavelength = 355 nm) of **5** and benzyl bromide (0.3 M) in deoxygenated toluene was recorded (Fig. 9c). Under this condition, the excited state of complex **5** is completely quenched by benzyl bromide within 4 μs. Therefore, the absorption bands at 457 and 552 nm observed at 4 μs after the laser flash should originate from photoreaction products. Referring to the absorption characteristics of Br$_2$ (390 nm),[19] Br$^-$ (<300 nm),[20] Br$_2^{\cdot-}$ (360/700 nm),[21] Br$_3^-$ (265 nm)[22] and PhCH$_2^\cdot$ (318/307 nm),[23] we exclude that the 457 nm and 552 nm absorption bands originate from the above species. At a high concentration of benzyl bromide (3 M), the excited state of **5** was completely quenched within 0.2 μs, and absorption bands at 457 and 552 nm were observed within 10 ns after the laser flash (Fig. S23†).

Absorption bands at 457 and 552 nm were also detected by laser flash photolysis of complex **5** in the presence of 4-(methoxycarbonyl)-*N*-methylpyridinium hexafluorophosphate and NBu$_4$Br. As shown in Fig. 9d, the TA spectrum at 300 ns after laser flash shows the characteristic absorption band of **5$^+$** at 820 nm. At later time after the laser flash (2–10 μs), an increase in the absorption bands at 457 and 552 nm is observed, with a concomitant decay at 820 nm, following a bi-exponential kinetics with τ_1 of 5.2 and τ_2 of 44.9 μs; the former lifetime can be related to the growth lifetime (3.0 μs) extracted from the

Fig. 8 UV-visible absorption spectra of (a) complex **1** and (b) complex **5** before and after the addition of 1 equiv. (TBPA)SbCl$_6$ in a mixed CH$_2$Cl$_2$/MeCN solution (2 : 1 v/v) at −40 °C. (c) X-band EPR spectrum (solid, black) of the reaction mixture of **1** (3 mM) and 0.5 equiv. (TBPA) SbCl$_6$ in frozen CH$_2$Cl$_2$ at 100 K; spectral simulation (dash, red) revealed that the spectrum comprises 75% Pd^{II}–Pd^{III} species (**1$^+$**) and 25% organic radicals. (d) X-band EPR spectrum of the reaction mixture of **5** (3 mM) and 0.5 equiv. (TBPA)SbCl$_6$ in frozen CH$_2$Cl$_2$ at 100 K. (e) ns-TA spectrum recorded at 1 μs after flashing a deoxygenated MeCN/ toluene (1 : 9 v/v) solution of complex **5** (2 × 10^5 s^{-1}) and 4-(methoxycarbonyl)-*N*-methylpyridinium hexafluorophosphate (0.001 M) at RT.

Table 4 Quenching rate constants of complex **5** by various alkyl bromides in deoxygenated toluene at RT

Alkyl bromide	E_{red}[a] [V]	BDE[b] [kcal mol^{-1}]	k_q [dm^3 mol^{-1} s^{-1}]
CBr$_4$	−0.41	50.8	7.17×10^9
Ethyl tribromoacetate	−0.49	58.9	2.55×10^9
Phenacyl bromide	−0.97	64.8	9.00×10^8
Bromodiphenyl methane	−1.08	—	1.52×10^8
Benzyl bromide	−1.30	57.1	1.57×10^7
Allyl bromide	−1.60	55.7	6.56×10^6
CH$_2$Br$_2$	−1.77	66.0	1.06×10^6

[a] Onset values of the cathodic peak in cyclic voltammogram (measured in DMF solution with 0.1 M NBu$_4$PF$_6$ vs. SCE). [b] Values of bond dissociation energy for the C–Br bond.

Fig. 9 (a) Correlation of the reduction potentials of alkyl bromides with log k_q of **5**. (b) Correlation of the BDE values of alkyl bromides with log(k_q/n) of **5**; n corresponds to the number of bromine atoms in alkyl bromides. (c) ns-TA spectra of complex **5** (2×10^{-5} M) in the presence of benzyl bromide (0.3 M) in deoxygenated toluene at RT. (d) ns-TA spectra of complex **5** (2×10^{-5} M) in the presence of 4-(methoxycarbonyl)-N-methylpyridinium hexafluorophosphate (0.001 M) and NBu$_4$Br (0.05 mM) in deoxygenated MeCN/toluene (1 : 9) at RT. (e) Decay of the TA signal at 820 nm for the photolysis reaction of complex **5** and 4-(methoxycarbonyl)-N-methylpyridinium hexafluorophosphate with and without NBu$_4$Br. (f) Decay of the TA signal at 457 nm for the photolysis reaction of complex **5** with 4-(methoxycarbonyl)-N-methylpyridinium hexafluorophosphate and NBu$_4$Br. (g) Dependence of decay rates of **5**$^+$ on the concentrations of NBu$_4$Br.

kinetics at 457 nm (Fig. 9f), showing a reaction between **5**$^+$ and Br$^-$ (eqn (3)). Increasing the NBu$_4$Br concentration further

$$[Pd^{II}(DPF^{0.5-})]_2^{3+} + Br^- \longrightarrow [(Pd^{II}\text{-}Pd^{III}\text{-}Br)(DPF\text{-})_2]^{2+} \quad (3)$$
$$(5^+) \qquad\qquad\qquad\qquad (5\text{-Br})$$

reduces τ_1, and the pseudo-first-order rate constant (k_{obs}) is linearly related to the NBu$_4$Br concentration, from which the second-order rate constant (k_2) could be determined to be 4.5 × 10^9 M^{-1} s^{-1} (Fig. 9g).

To further identify the photoreaction products, the EPR spectra of the photolysis mixture of **5** and benzyl bromide in frozen benzene were recorded at 100 K. An EPR signal attributable to the combined signal of Pd compounds **[Pd]** (20%) and organic radicals (80%) was observed (Fig. 10a). Spectral

simulations gave the following parameters for the $S = 1/2$ **[Pd]** species: $g_{\parallel} = 2.029$, $g_{\perp} = 1.990$, $A_{\parallel} = 8$ G, $A_{\perp} = 3$ G. The low g-anisotropy ($\Delta g = 0.039$) and small deviation of g_{av} (2.0030) from the free electron g value (2.0023) indicate that the unpaired electron of **[Pd]** is partially distributed on the ligand.[24] Furthermore, the order $g_{\parallel} > g_{\perp}$ suggests that the unpaired electron also has some Pd characters residing in d$_{xz}$/d$_{yz}$ or d$_{x^2-y^2}$-based orbitals.[24,25] DFT calculations were performed to reveal the electronic structure of **5**$^+$ and **5-Br**. As shown in Fig. 10b, the calculated spin densities of Pd1 and Pd2 atom in **5**$^+$ are the same, both are 0.04. The calculated spin density on the four N1, N2, N3 and N4 atoms of **5**$^+$ is much larger than that of the Pd atom, totaling 0.7, showing that the unpaired electron is mainly located at the formamidinate ligand. This calculation result is consistent with the EPR characteristic of **5**$^+$ generated
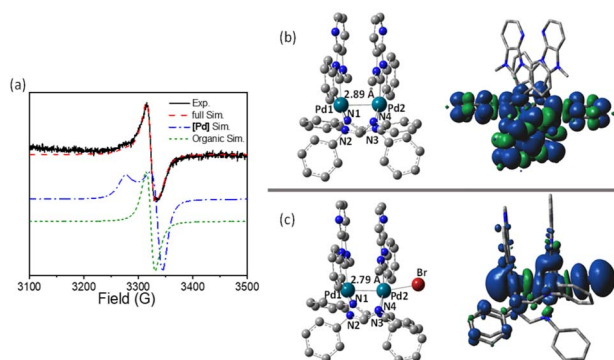
Fig. 10 (a) X-band EPR spectrum and simulation of the reaction mixture of **5** and benzyl bromide in frozen benzene at 100 K after light irradiation for 15 minutes. (b) Optimized structure (left) and spin density population (right) of complex **5⁺**. (c) Optimized structure (left) and spin density population (right) of complex **5-Br**.

by chemical oxidation of **5** with (TBPA)SbCl₆ (Fig. 8d). The Pd–Pd distance shrinks from 2.89 Å in **5** to 2.79 Å in **5-Br** (Fig. 10c), showing Pd–Pd bonding interactions (though weak) due to the oxidation of Pd atoms. The spin density distribution of **5-Br** is mainly localized on Pd and Br atoms, and the values of Pd1, Pd2 and Br atom are 0.14, 0.4 and 0.29, respectively. This significant difference in the spin density population between **5-Br** and **5⁺** is consistent with the different EPR patterns of **5-Br** and **5⁺**.

There are three possible reaction mechanisms for the photoreaction of binuclear Pd^{II} complex **5** with alkyl bromides, as shown in Scheme 1:[26] (1) in the outer-sphere electron transfer mechanism, the alkyl bromide R–Br receives electrons from the excited state of **5** and undergoes C–Br bond cleavage to generate the bromide anion, which is subsequently added to the metal center; (2) the inner-sphere electron transfer reaction involves the formation of caged ion pairs as intermediates prior to the electron transfer process; (3) alternatively, the excited state of **5** can react with alkyl bromides through a halogen atom abstraction mechanism. The linear correlation between the log k_q values of **5** and the reduction potentials of the alkyl bromides is inconsistent with the halogen atom abstraction hypothesis, which predicts that the reaction rate depends on the BDE of the alkyl bromide. No formation of **5⁺** was observed in laser flash
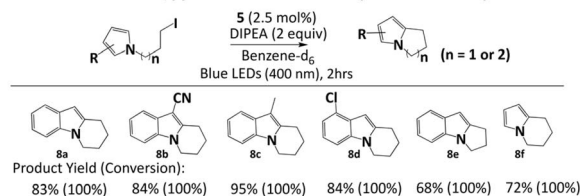
photolysis experiments of **5** with benzyl bromide, whereas the direct observation of **5-Br** on the nanosecond time scale suggests that the reaction most likely follows an inner-sphere electron transfer mechanism.
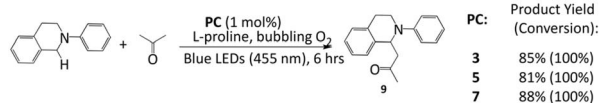
Photocatalysis

The bimolecular photoreaction between **5** and alkyl halides prompts us to study the application of **5** as a photocatalyst in the photo-induced intramolecular cyclization of indole/pyrrole (Scheme 2).[27] For all substrates examined, 100% substrate conversion and high yields of cyclized products (68–95%) were achieved (Scheme 2). Both electron-rich indoles and electron-deficient indoles perform well in photo-induced cyclization reactions. Notably, the C3 electron-rich indole gave the highest product yield (95%). The conversion efficiency of 1-(3-iodo-propyl)-1H-indole to the cyclized product was less satisfactory (68%), probably due to the higher ring strain of the five-membered fused ring than the six-membered fused ring. This photoredox reaction also worked for pyrrole, furnishing the cyclized product in 72% yield.

With $E(\text{DIPEA}^+/\text{DIPEA}^0) = 0.65$ V vs. SCE and E_{red} of 1-(4-iodobutyl)-1H-indole $= -1.68$ V vs. SCE, the oxidative quenching of *5 by 1-(4-iodobutyl)-1H-indole is thermodynamically favored by 0.20 V and the reductive quenching of *5 by DIPEA is thermodynamically uphill by 0.13 V. Stern–Volmer quenching experiments showed that 1-(4-iodobutyl)-1H-indole quenches the emission of **5** with a k_q of 1.65×10^7 M⁻¹ s⁻¹, while the quenching of the emission of **5** by DIPEA is negligible (Fig. S24†). In addition, we observed a long-lived species ($\tau > 10$ μs) in the ns-TA spectrum of a deoxygenated toluene solution
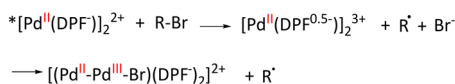

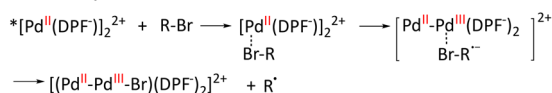Scheme 2 Photo-induced indoles/pyrroles functionalization by intramolecular cyclization (upper), and aerobic C–C coupling reactions of N-phenyl-1,2,3,4-tetrahydroisoquinoline with acetone (bottom). 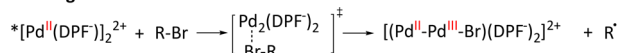(a) Reaction conditions: indoles/pyrroles (0.05 mmol), DIPEA (0.10 mmol), complex **5** (2.5 mol%) in 0.56 mL deoxygenated benzene-d₆, light (LED lamp, $\lambda_{max} = 400$ nm, 24 W), irradiation time: 2 h. (b) Reaction conditions: N-phenyl-1,2,3,4-tetrahydroisoquinoline (0.128 mmol), acetone (0.4 mL), L-proline (0.128 mmol), PC (1 mol%), MeCN (0.4 mL), MeOH (0.8 mL), oxygen, light (LED lamp, $\lambda_{max} = 455$ nm, 24 W), irradiation time: 6 h. Product yields and substrate conversion were calculated by ¹H NMR using 1,3,5-trimethoxybenzene as an internal standard.

Scheme 1 Possible reaction mechanisms for the photoreaction of complex **5** with alkyl bromides.

Fig. 11 (a) ns-TA spectra at 0.01 and 4 μs after flashing a deoxygenated toluene solution of **5** (2×10^{-5} M). (b) ns-TA spectra at 0.01 and 4 μs after flashing a deoxygenated toluene solution containing **5** (2×10^{-5} M) and 1-(4-iodobutyl)-1*H*-indole (0.1 M). (c) Photoreaction of 1-(4-iodobutyl)-1*H*-indole in the presence of TEMPO. Product yield was calculated by ^{1}H NMR using 1,3,5-trimethoxybenzene as an internal standard.
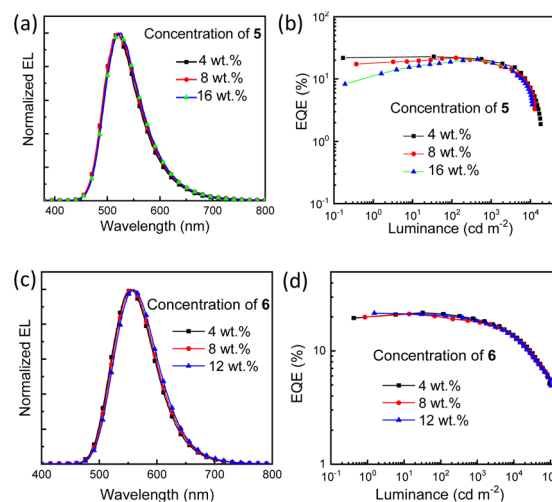
containing **5** and 1-(4-iodobutyl)-1*H*-indole (Fig. 11b). This shows that the photoreaction is initiated by oxidative quenching of ***5** with indole. Photoreaction of 1-(4-iodobutyl)-1*H*-indole in the presence of TEMPO (2,2,6,6-tetramethyl-1-piperidyloxy) as a scavenger was conducted; the TEMPO-coupling product was obtained in 90% yield (Fig. 11c). In view of the above results, a plausible reaction mechanism was proposed and shown in Fig. S25.† The mixed ^{3}MMLCT/^{3}LLCT excited state of **5** can induce reductive dehalogenation of *N*-alkylated indole/pyrrole to form an alkyl radical, which subsequently undergoes cyclization reaction to give a benzylic radical. Oxidation of the benzylic radical followed by deprotonation affords the desired cyclized product. DIPEA was used as a sacrificial electron donor to regenerate **5**.

The feasibility of these binuclear Pd^{II} complexes as photosensitizers (PC) was also examined in the photochemical generation of singlet oxygen (^{1}O$_2$). As shown in Fig. S26,† the emission of ^{1}O$_2$ was detected upon photoexcitation of binuclear Pd^{II} complexes (**3**, **5**, and **7**) in aerated CHCl$_3$. Referring to the emission intensity of ^{1}O$_2$ produced with H$_2$tpp as the photosensitizer ($\Phi_{so} = 0.55$ in CHCl$_3$) at $\lambda_{max} = 1270$ nm,[28] it was found that the Φ_{so} values of **3**, **5**, and **7** were 0.19, 0.15 and 0.08, respectively. Subsequently, we examined the photo-induced aerobic C–C coupling reaction of *N*-phenyl-1,2,3,4-tetrahydroisoquinoline with acetone using these complexes as photosensitizers. This reaction is known to be initiated by the oxidation of amines to iminium ion intermediates *via* photochemically generated ^{1}O$_2$.[29] As shown in Scheme 2, complete substrate conversion (100%) and high product yields (81–88%) were achieved. Control experiments showed that in the absence of binuclear Pd^{II} complexes, L-proline, O$_2$ or light irradiation, only trace amounts of coupling products were detected.

Electroluminescence

The high emission quantum yields of **5** and **6** in PMMA thin films prompted us to investigate their potential applications as

OLED emitters. Devices with architecture consisting of ITO/HAT-CN (5 nm)/TAPC (40 nm)/CCP (10 nm)/**5**: PPF (10 nm)/PPF (10 nm)/TmPyPb (40 nm)/LiF (1.2 nm)/Al (100 nm) were fabricated to examine the electroluminescent (EL) properties of **5**. In these devices, di-[4-(*N*,*N*-ditolyl-amino)-phenyl] cyclohexane (TAPC) and 1,3,5-tri(*m*-pyrid-3-yl-phenyl)benzene (TmPyPb) were used as the hole-transporting layer (HTL) and electron-transporting layer (ETL), respectively, and 1,4,5,8,9,11-hexaazatriphenylene hexacarbonitrile (HAT-CN) was used as the hole-injecting layer to facilitate the hole injection from ITO to TAPC. Complex **5** was doped in 2,8 bis(diphenylphosphoryl) dibenzo[*b*,*d*]furan (PPF) at concentrations ranging from 4 to 16 wt% to form an emissive layer (EML). PPF and CCP (9-phenyl-3,9′-bicarbazole), with triplet energies of 3.0 and 3.1 eV, were used as an exciton-blocking layer to confine the excitons within the EML.[30] When the doping concentration is 4 wt%, the EL maximum of **5** is located at 521 nm (Fig. 12a). When the doping concentration is increased to 8 wt%, the EL spectrum of **5** is almost unchanged and is slightly red-shifted to 525 nm at 16 wt%. The device with 4 wt% of **5** achieved a high max. EQE of 22.9% (Fig. 12b), corresponding to a current efficiency (CE) of 71.2 cd A^{-1} (Table 5). At high luminance of 1000 cd m^{-2}, the EQE and CE of this device slightly dropped to 19.6% and 60.9 cd A^{-1}, respectively. In devices with 8 wt% and 16 wt% doping concentrations of **5**, max. EQE values dropped slightly to 21.8% and 20.7%, respectively. Although the PLQY (0.92–0.93) of **5** in PPF is similar at different doping concentrations (Fig. S27†), the luminance and EQE at 1000 cd m^{-2} of devices with higher concentrations of **5** are lower than those with 4 wt% of **5**. The inferior device performance of **5**-based devices at higher doping concentrations can be attributed to the strong trapping effect of **5**, as shown in Fig. S28.† The HOMO energy level (−5.2 eV) of **5** is 1.5 eV higher than the host PPF (−6.7 eV), causing holes injected from the HTL deeply trapped.

Fig. 12 (a) Normalized EL spectra and (b) EQE-luminance characteristics of OLEDs with **5** at various doping concentrations. (c) Normalized EL spectra and (d) EQE-luminance characteristics of OLEDs with **6** at various doping concentrations.

Table 5 Key performances of OLEDs with **5** and **6** at various concentrations[a]a

	L_{max}[b] [cd m^{-2}]	Max. EQE[c] [%]	EQE[c] at 1000 cd m^{-2} [%]	Max. CE[d] [cd A^{-1}]	Max. PE[e] [lm W^{-1}]	CIE coordinates[f] (x, y)
PPF: **5** (4 wt%)	18 200	22.9	19.6	71.2	85.2	0.29, 0.57
PPF: **5** (8 wt%)	12 750	21.8	18.4	70.2	70.0	0.30, 0.57
PPF: **5** (16 wt%)	11 200	20.7	18.2	64.1	39.5	0.31, 0.58
mCBP: **6** (4 wt%)	94 100	21.8	18.9	76.5	61.9	0.41, 0.56
mCBP: **6** (8 wt%)	99 100	21.2	17.9	73.8	62.3	0.42, 0.56
mCBP: **6** (12 wt%)	104 000	21.5	18.4	73.4	65.9	0.43, 0.55

[a] Fabricated by vacuum deposition. [b] Max. luminance. [c] External quantum efficiency. [d] Current efficiency. [e] Power efficiency. [f] CIE coordinates at 1000 cd m^{-2}.

For **6**-based OLEDs, EML is formed by doping **6** in mCBP (3,3′-di(9H-carbazol-9-yl)-1,1′-biphenyl) at a concentration of 4 to 12 wt%. As shown in Fig. 12c, the EL spectrum of the **6**-based device is unstructured with a peak maximum at 554–560 nm. The max. luminance and max. power efficiency (PE) increase as the doping concentration increases from 4 wt% to 12 wt%, up to 104 000 cd m^{-2} and 69.5 lm W^{-1}, respectively. The max. EQE values (21.2–21.8%) are almost insensitive to the doping concentration (Fig. 12d). The OLED performance of complex **5** is slightly inferior to that of the Pt^{II} analogue; the max. EQE of the latter is reported to be over 25%.[31] Nevertheless, the max. EQE and max. luminance of the **5**-based OLEDs are up to 22.9% and 104 000 cd m^{-2}, respectively; these two values are the highest among OLEDs doped with binuclear Pd^{II} emitters.[6] At high luminance of 1000 cd m^{-2}, the EQE values drop slightly to 17.9–18.9%, corresponding to an efficiency roll-off of 13.3–15.6%.

Conclusion

In this work, binuclear Pd^{II} complexes with short intramolecular Pd–Pd distances of 2.79–2.89 Å and ^{3}MMLCT excited state with high Φ_{em} (up to 0.7) and large k_r (up to 2×10^5 s^{-1}) have been achieved. These binuclear Pd^{II} complexes show potential applications as light-emitting dopants for OLEDs and as photocatalysts or photosensitizers for C–C coupling reactions. According to DFT/TDDFT calculations, the energy difference between the ^{3}MMLCT and ^{3}dd excited states of complex **1** is smaller than that of **Ref-Pt1**. Together with the smaller SOC, complex **1** shows faster non-radiative decay and slower radiative decay processes. The strongly σ-donating (C^C*) ligands of complexes **5** and **6** can significantly destabilize the ^{3}dd excited state. Complex **5** reacts with alkyl bromide through the inner-sphere electron transfer pathway under photo-irradiation, and the Pd-containing product is $[(Pd^{II}–Pd^{III}–Br)(DPF^-)_2]^{2+}$ (**5-Br**). Overall, this work provides a comprehensive study of the ^{3}MMLCT excited states of binuclear Pd^{II} complexes from basic research to applications.

Data availability

The data supporting this article have been included as part of the ESI.†

Author contributions

Chi-Ming Che designed and initiated this research project. Minying Xue synthesized and characterized all complexes in this work, performed the spectroscopic and electrochemical measurements and carried out the photochemical studies. Wai-Pong To provided experimental guidance for this research project. Chi-Ming Che, Qingyun Wan and Minying Xue wrote and revised the manuscript. Yuzhen Zhang grew the single crystals of complex **1** and **Ref-Pt1**. Gang Cheng performed OLED fabrication and electroluminescence measurements. Zhou Tang carried out the EPR simulations. Lili Du carried out the femtosecond time-resolved absorption and emission spectroscopic measurements. Kam-Hung Low was responsible for X-ray crystal structure determinations. Qingyun Wan was responsible for all the DFT/TDDFT calculations in this work.

Conflicts of interest

There are no conflicts to declare.

Acknowledgements

References

1 (a) M. Yoshida and M. Kato, *Coord. Chem. Rev.*, 2018, **355**, 101–115; (b) S.-Y. Yang, Y. Chen, R. T. K. Kwok, J. W. Y. Lam and B. Z. Tang, *Chem. Soc. Rev.*, 2024, **53**, 5366.

2 (a) M. Han, Y. Tian, Z. Yuan, L. Zhu and B. Ma, *Angew. Chem.*, 2014, **126**, 11088; *Angew. Chem., Int. Ed.*, 2014, **53**, 10908; (b) X.-P. Zhang, J.-F. Mei, J.-C. Lai, C.-H. Li and X.-Z. You, *J. Mater. Chem. C*, 2015, **3**, 2350; (c) J. Ni, Y. Zhang, S. Liu

and J. Zhang, *J. Organomet. Chem.*, 2024, **1004**, 122948; (*d*) J. Ni, Q. Zhu, X. Wang, S. Liu and J. Zhang, *J. Organomet. Chem.*, 2024, **1015**, 123233.

3 (*a*) K. T. Ly, R.-W. Chen-Cheng, H.-W. Lin, Y.-J. Shiau, S.-H. Liu, P.-T. Chou, C.-S. Tsao, Y.-C. Huang and Y. Chi, *Nat. Photonics*, 2017, **11**, 63; (*b*) K.-H. Kim, J.-L. Liao, S. W. Lee, B. Sim, C.-K. Moon, G.-H. Lee, H. J. Kim, Y. Chi and J.-J. Kim, *Adv. Mater.*, 2016, **28**, 2526; (*c*) P. Pinter, J. Soellner and T. Strassner, *Eur. J. Inorg. Chem.*, 2021, 3104; (*d*) H. Leopold, M. Tenne, A. Tronnier, S. Metz, I. Münster, G. Wagenblast and T. Strassner, *Angew. Chem.*, 2016, **128**, 16011; *Angew. Chem., Int. Ed.*, 2016, **55**, 15779; (*e*) M. Xue, T.-L. Lam, G. Cheng, W. Liu, K.-H. Low, L. Du, S. Xu, F.-F. Hung, D. L. Phillips and C.-M. Che, *Adv. Opt. Mater.*, 2022, **10**, 2200741.

4 (*a*) V. Sicilia, L. Arnal, S. Fuertes, A. Martín and M. Baya, *Inorg. Chem.*, 2020, **59**, 12586; (*b*) V. Sicilia, P. Borja and A. Martín, *Inorganics*, 2014, **2**, 508; (*c*) V. Sicilia, M. Baya, P. Borja and A. Martín, *Inorg. Chem.*, 2015, **54**, 7316.

5 (*a*) J. J. Topczewski and M. S. Sanford, *Chem. Sci.*, 2015, **6**, 70; (*b*) D. C. Powers and T. Ritter, *Acc. Chem. Res.*, 2012, **45**, 840; (*c*) D. C. Powers, M. A. L. Geibel, J. E. M. N. Klein and T. Ritter, *J. Am. Chem. Soc.*, 2009, **131**, 17050; (*d*) D. C. Powers and T. Ritter, *Nat. Chem.*, 2009, **1**, 302.

6 (*a*) J. Lin, C. Zou, X. Zhang, Q. Gao, S. Suo, Q. Zhuo, X. Chang, M. Xie and W. Lu, *Dalton Trans.*, 2019, **48**, 10417; (*b*) L. Qiao, X. Kong, K. Li, L. Yuan, Y. Shen, Y. Zhang and L. Zhou, *Adv. Sci.*, 2024, 2404621.

7 P. K. Chow, C. Ma, W.-P. To, G. S. M. Tong, S.-L. Lai, S. C. F. Kui, W.-M. Kwok and C.-M. Che, *Angew. Chem., Int. Ed.*, 2013, **52**, 11775.

8 (*a*) Q. Wan, W.-P. To, C. Yang and C.-M. Che, *Angew. Chem.*, 2018, **130**, 3143; *Angew. Chem., Int. Ed.*, 2018, **57**, 3089; (*b*) C. Zou, J. Lin, S. Suo, M. Xie, X. Chang and W. Lu, *Chem. Commun.*, 2018, **54**, 5319; (*c*) L. Cao, K. Klimes, Y. Ji, T. Fleetham and J. Li, *Nat. Photonics*, 2019, **15**, 185; (*d*) L. Ameri, L. Cao, X. Tan and J. Li, *Adv. Mater.*, 2023, **35**, 2208361.

9 J. Pérez, A. Espinosa, J. M. Galiana, E. Pérez, J. L. Serrano, M. A. G. Aranda and M. Insausti, *Dalton Trans.*, 2009, 9625.

10 B. Ma, J. Li, P. I. Djurovich, M. Yousufuddin, R. Bau and M. E. Thompson, *J. Am. Chem. Soc.*, 2005, **127**, 28.

11 (*a*) P.-K. Chow, G. Cheng, G. S. M. Tong, C. Ma, W.-M. Kwok, W.-H. Ang, C. Y.-S. Chung, C. Yang, F. Wang and C.-M. Che, *Chem. Sci.*, 2016, **7**, 6083; (*b*) G. Li, J. Zheng, X. Fang, K. Xu, Y.-F. Yang, J. Wu, L. Cao, J. Li and Y. She, *Organometallics*, 2021, **40**, 472; (*c*) G. Li, H. Guo, X. Fang, Y.-F. Yang, Y. Sun, W. Lou, Q. Zhang and Y. She, *Chin. J. Chem.*, 2022, **40**, 223.

12 J. Liu, T.-L. Lam, M.-K. Sit, Q. Wan, C. Yang, G. Cheng and C.-M. Che, *J. Mater. Chem. C*, 2022, **10**, 10271.

13 P. S. Wagenknecht and P. C. Ford, *Coord. Chem. Rev.*, 2011, **225**, 591.

14 (*a*) M. Chaaban, Y.-C. Chi, M. Worku, C. Zhou, H. Lin, S. Lee, A. Ben-Akacha, X. Lin, C. Huang and B. Ma, *Inorg. Chem.*, 2020, **59**, 13109; (*b*) S. F. Wang, L. W. Fu, Y.-C. Wei, S.-H. Liu, J.-A. Lin, G.-H. Lee, P.-T. Chou, J.-Z. Huang, C.-I. Wu, Y. Yuan, C.-S. Lee and Y. Chi, *Inorg. Chem.*, 2019, **58**, 13892.

15 H. Amouri, *Chem. Rev.*, 2023, **123**, 230.

16 C.-L. Yao, L.-P. He, J. D. Korp and J. L. Bear, *Inorg. Chem.*, 1988, **27**, 4389.

17 J. F. Berry, E. Bill, E. Bothe, F. A. Cotton, N. S. Dalal, S. A. Ibragimov, N. Kaur, C. Y. Liu, C. A. Murillo, S. Nellutla, J. M. North and D. Villagrán, *J. Am. Chem. Soc.*, 2007, **129**, 1393.

18 C.-H. Lam, W. K. Tang and V. W.-W. Yam, *Inorg. Chem.*, 2023, **62**, 1942.

19 N. Bayliss, A. Cole and B. Green, *Aust. J. Chem.*, 1948, **1**, 472.

20 M. Hermet, L. Bakás, S. R. Morcelle and D. L. Bernik, *Spectrochim. Acta, Part A*, 2019, **223**, 117266.

21 S. Yamashita, K. Iwamatsu, Y. Maehashi, M. Taguchi, K. Hata, Y. Muroya and Y. Katsumura, *RSC Adv.*, 2015, **5**, 25877.

22 M. Dey, S. S. Dhar and M. Kalita, *Synth. Commun.*, 2013, **43**, 1734.

23 (*a*) J. P. Mittal and E. Hayon, *Nat. Phys. Sci.*, 1972, **240**, 20; (*b*) N. A. McAskill and D. F. Sangster, *Aust. J. Chem.*, 1977, **30**, 2107.

24 S. H. Eitel, M. Bauer, D. Schweinfurth, N. Deibel, B. Sarkar, H. Kelm, H.-J. Kruger, W. Frey and R. Peters, *J. Am. Chem. Soc.*, 2012, **134**, 4683.

25 J. Harmer, C. Finazzo, R. Piskorski, C. Bauer, B. Jaun, E. C. Duin, M. Goenrich, R. K. Thauer, S. V. Doorslaer and A. Schweiger, *J. Am. Chem. Soc.*, 2005, **127**, 17744.

26 (*a*) D. C. Smith and H. B. Gray, *Coord. Chem. Rev.*, 1990, **100**, 169; (*b*) S. J. Atherton and D. M. Roundhill, *Inorg. Chem.*, 1986, **25**, 4072.

27 S. J. Kaldas, A. Cannillo, T. McCallum and L. Barriault, *Org. Lett.*, 2015, **17**, 2864.

28 F. Wilkinson, W. P. Helman and A. B. Ross, *J. Phys. Chem. Ref. Data*, 1993, **22**, 113.

29 W.-P. To, Y. Liu, T.-C. Lau and C.-M. Che, *Chem.–Eur. J.*, 2013, **19**, 5654.

30 (*a*) M. Numata, T. Yasuda and C. Adachi, *Chem. Commun.*, 2015, **51**, 9443; (*b*) I. S. Park, K. Matsuo, N. Aizawa and T. Yasuda, *Adv. Funct. Mater.*, 2018, **28**, 1802031.

31 (*a*) T.-L. Lam, H. Li, K. Tan, Z. Chen, Y.-K. Tang, J. Yang, G. Cheng, L. Dai and C.-M. Che, *Small*, 2024, **20**, 2307393; (*b*) L. Wang, J. Miao, Y. Zhang, C. Wu, H. Huang, X. Wang and C. Yang, *Adv. Mater.*, 2023, **35**, 2303066.